1.5.5.3.3.4 $C1_b$ compounds

XYZ X = 3d, 4d, 5d, Y = 3d

X = 8A: Co, Ni, Ir, Pd, Pt; 1B: Cu, Ag, Au
Y = 7A: Mn
Z = 4B: Sn

The investigation of the magnetic properties of these compounds has been primarily motivated by their potential use as thermomagnetic recording materials. The majority of the compounds are ferromagnetic although those with X = Cu or Ir are antiferromagnetic.

Table 26. Summary of the magnetic properties of some $C1_b$ compounds [87O3].

	CoMnSb	NiMnSb	CuMnSb	PtMnSb	AuMnSb	PtMnSn
Unit cell [Å]	2×5.875	5.927	6.095	6.195	6.373	6.261
Magnetic order	F	F	AF	F	F	F
T_C or T_N [K]	478	728	55	572	72	330
Θ [K]	490 - 530	780 - 910	– 160	610 - 670	98	350
p_s(0K) [μ_B]	4.2	4.2	3.9	4.0	3.5	3.5
p_{eff} [μ_B]	4.6 - 4.0	4.2 - 2.9	5.4	4.9 - 4.3	5.7	5.2

Table 27. A summary of structural, magnetic and the pressure dependence of the Curie temperature in some ferromagnetic C1b and $L2_1$ compounds [83K1].

Substance	Crystal structure	Lattice constant [Å]	$D_{Mn–Mn}$ [Å]	$D_{Mn–Mn}/r_d$	T_C [K]	dT_C/dp [K/kbar]
PtMnSn	C1b	6.263	4.43	5.18	355	0.86
Ni_2MnSn	Heusler	6.04	4.27	4.99	342	0.55
Ni_2MnSb	Heusler	6.00	4.24	4.96	334	3
$Cu_2Mn_{1.2}In_{0.8}$	Heusler	6.19	4.38	5.12	449	1.5
Au_4Mn	tetragonal	4.02, 4.07	4.02	4.7	332	2.7
MnBi	NiAs	4.286, 4.116	3.06	3.58	613	– 5
MnSb	NiAs	4.128, 5.789	2.9	3.39	587	– 3.2
MnAs	NiAs	3.71, 5.69	2.85	3.33	312	– 12
MnP	MnP	3.173, 5.260 5.917	2.63	3.08	291	– 1.3

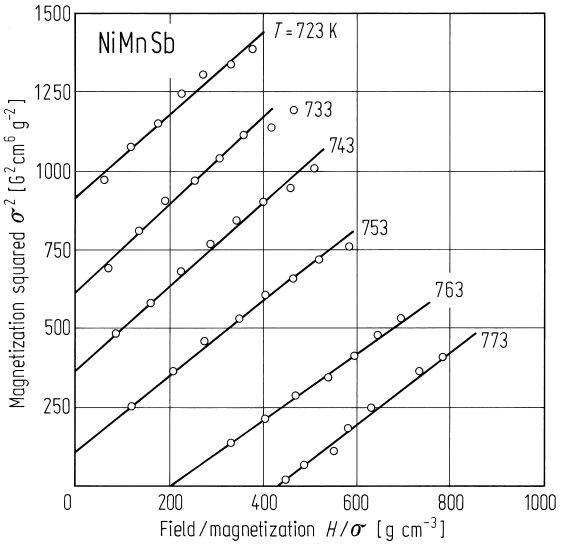

Fig. 143. Arrott plot for NiMnSb indicating a magnetically homogenous system [84H1].

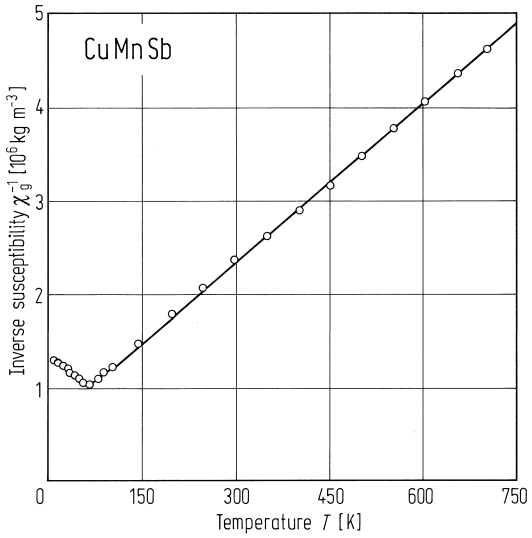

Fig. 144. Temperature dependence of the reciprocal susceptibility in CuMnSb [84H1].

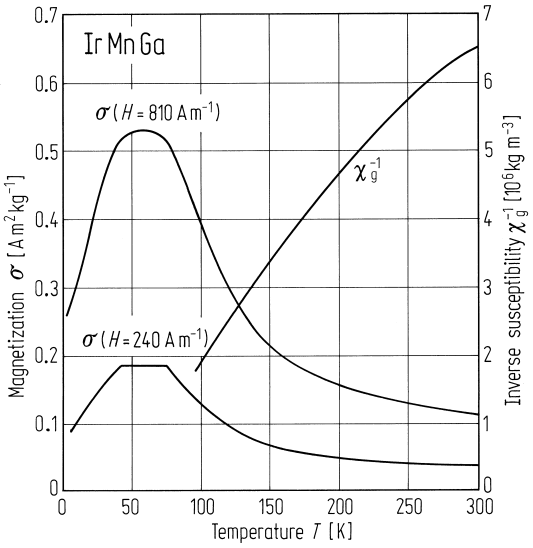

Fig. 145. Temperature dependence of the magnetisation σ (240 and 810 A/m) and the reciprocal susceptibility χ_g^{-1} in IrMnGa [84H1].

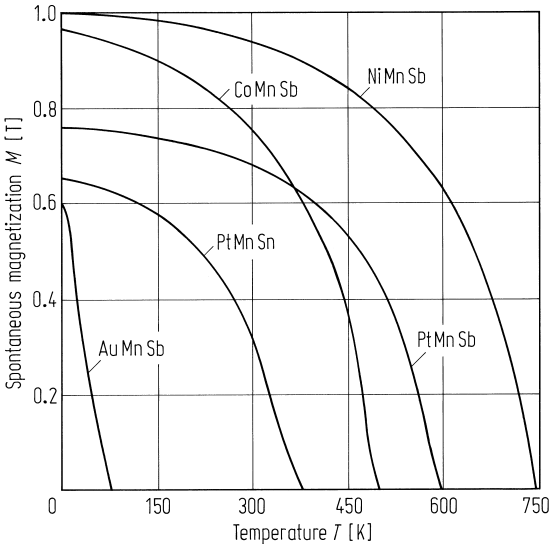

Fig. 146. Spontaneous magnetisation M as a function of temperature for several $C1_b$ compounds [87O3].

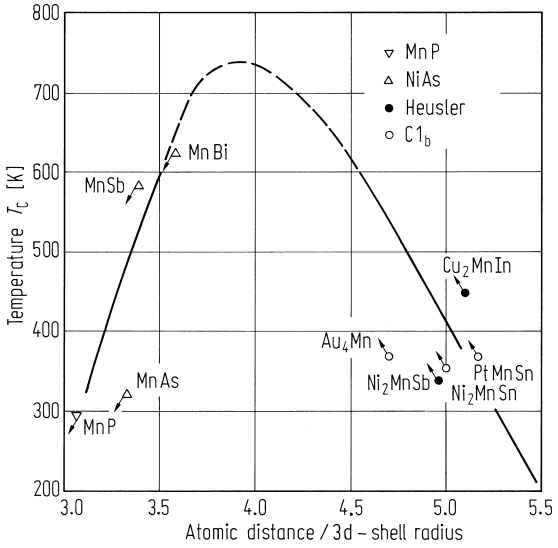

Fig. 147. Dependence of Curie temperature on Mn-Mn distance for some $L2_1$ and $C1_b$ Heusler alloys [83K1].

Lanthanide compounds with group 3d and 4d elements

$X_2(R)Z$

The main interest in these compounds centres on possible heavy Fermion behaviour or the co-existence of superconductivity and long-range magnetic order. In most compounds the lanthanide element occupies the Y site, although a new series has been reported in which they occupy the X sites.

Table 28. A summary of the crystallographic and magnetic properties of $(R)InCu_2$ compounds [85F1].

Compound	$a \pm 0.003$ [Å]	$T_N \pm 1$ [K]	$\Theta \pm 2$ [K]	p_{eff} (exp) ± 0.05 [μ_B]	p_{eff} (calc) [μ_B]	χ_0 [$cm^3\,mol^{-1}$]
$LaInCu_2$	6.856	Pauli paramagnet				$4.0\cdot10^{-3}$
$CeInCu_2$	6.798		– 30	2.52	2.54	$7.5\cdot10^{-3}$
$PrInCu_2$	6.774		– 35	3.53	3.58	$2.0\cdot10^{-3}$
$NdInCu_2$	6.746		– 70	2.60	3.62	$4.6\cdot10^{-3}$
$SmInCu_2$	6.691	7	No Curie-Weiss behaviour			
$GdInCu_2$	6.447	12	– 31	7.60	7.94	
$TbInCu_2$ *)	6.616	6	– 33	9.70	9.72	
$DyInCu_2$	6.601	3	– 21	10.30	10.63	
$ErInCu_2$ *)	6.552		– 10	9.63	9.59	
$LuInCu_2$	6.515					$-3\cdot10^{-4}$

*) Contain ≈ 10 % $MgCu_2$ cubic phase.

Table 29. A summary of the magnetic properties of X_2GdIn alloys [93N1].

Alloy	T_N [K]	Θ [K]	p_{eff} [μ_B]	a [Å]	Structure
Cu_2GdIn	10	– 58.8	7.89	6.641	$L2_1$
Ag_2GdIn	10	– 56	8.1	6.965	$L2_1$
Pd_2GdIn	≈ 7	5.64	8.22	6.741	$L2_1$

Table 30. Properties of some $CeInAg_{2-x}Cu_x$ compounds. p_{eff} was obtained from data above 150 K [87L1].

x	a [Å]	Θ [K]	T_N [K]	p_{eff} [μ_B]
2.0	6.784	– 30	< 0.5	2.60
1.9	6.800	– 26	2.2	2.56
1.8	6.830	– 25	3.5	2.535
1.7	6.845	– 22	4.0	2.535
1.5	6.891	– 18.5	5.5	2.53
1.0	6.967	– 12.5	4.0	2.535
0.0	7.108	– 9.0	2.7	2.54

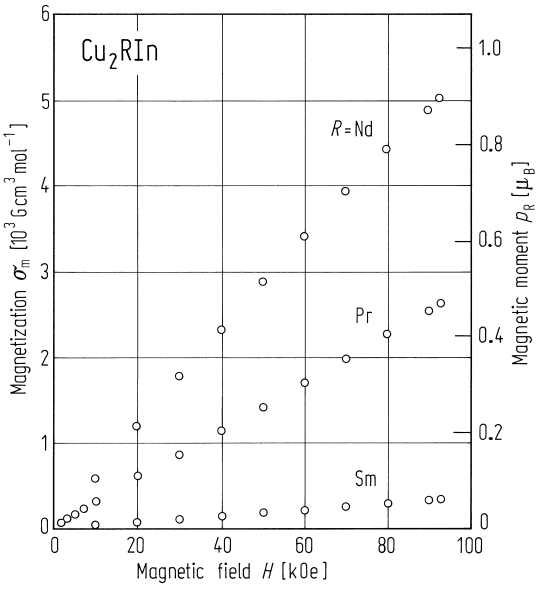

Fig. 148. Magnetisation of rare earth Heusler compounds Cu_2RIn (R = Nd, Pr, Sm) with a field of up to 9.5 T applied along (100) at 4.2 K [91S1].

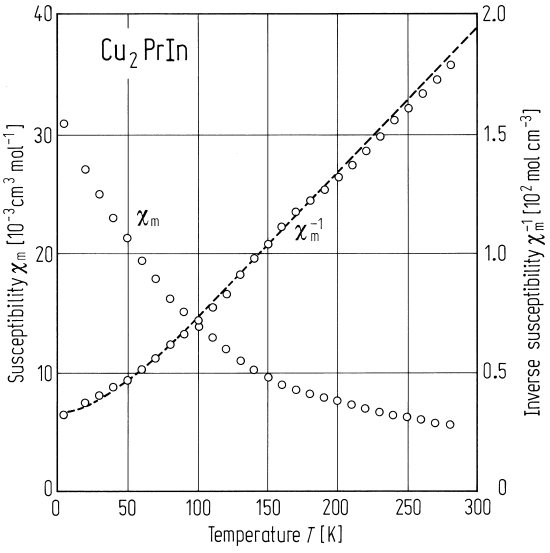

Fig. 149. Temperature dependence of susceptibility and inverse susceptibility of Cu_2PrIn with the applied field along (100) [91S1].

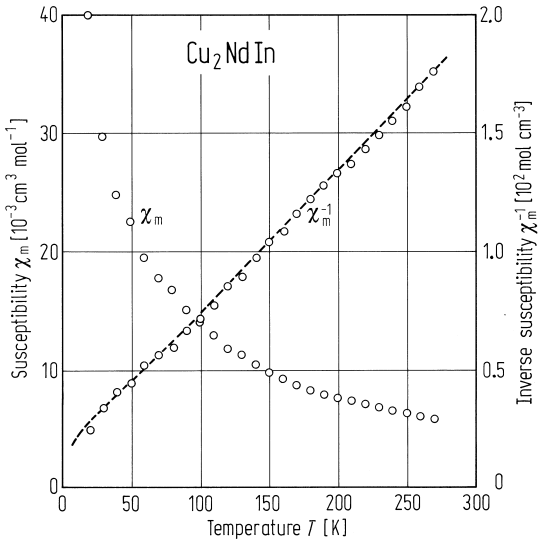

Fig. 150. Temperature dependence of susceptibility and inverse susceptibility of Cu_2NdIn with the applied field along (100) [91S1].

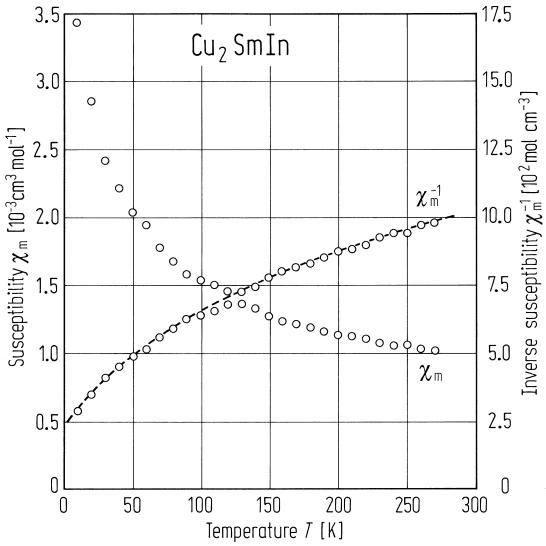

Fig. 151. Temperature dependence of susceptibility and inverse susceptibility of Cu_2SmIn with the field applied along (100) [91S1].

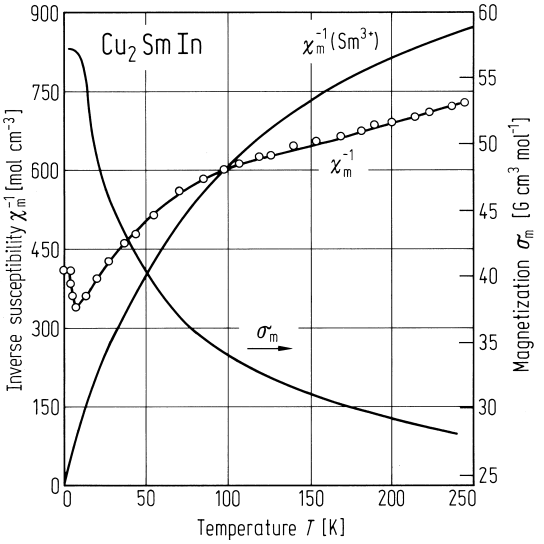

Fig. 152. Temperature dependence of the magnetisation and reciprocal susceptibility of Cu_2SmIn. For comparison the theoretical susceptibility of the free Sm^{3+} ion is also shown [85F1].

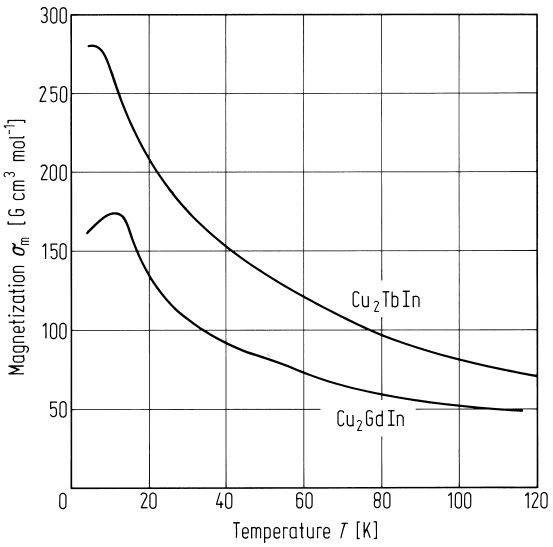

Fig. 153. Temperature dependence of the magnetisation at H = 1 kOe for Cu_2GdIn and Cu_2TbIn [85F1].

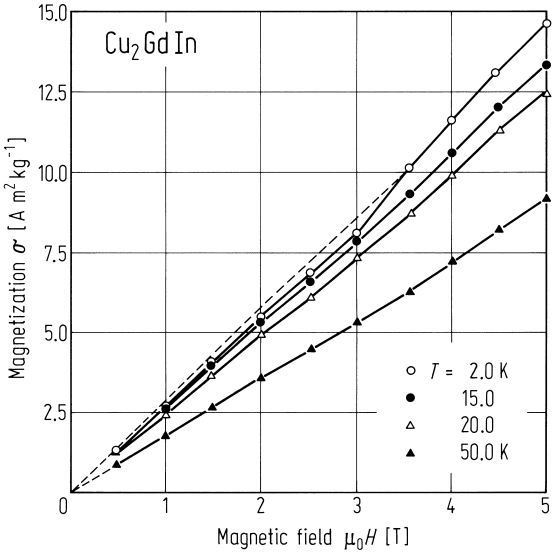

Fig. 154. Magnetisation of Cu_2GdIn as a function of magnetic field [93N1].

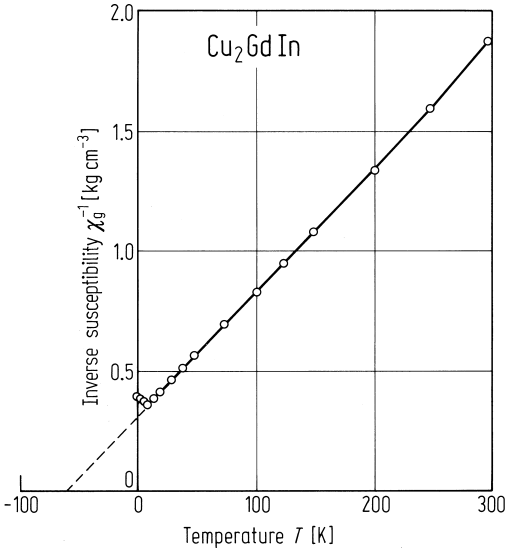

Fig. 155. Reciprocal susceptibility vs. temperature of Cu_2GdIn measured in a field of 0.5 T [93N1].

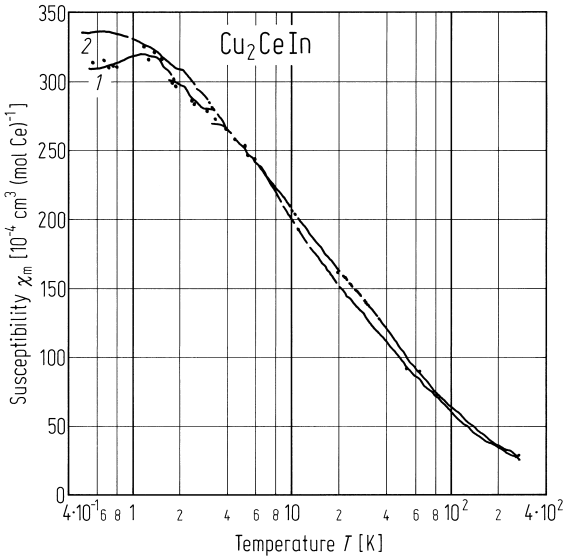

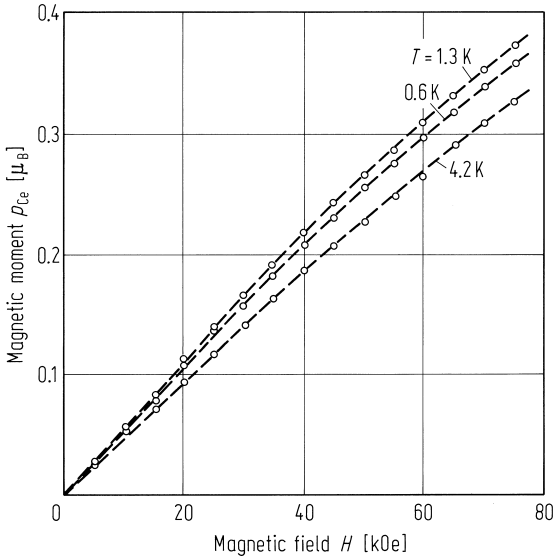

Fig. 157. Temperature dependence of the magnetic susceptibility for (*1*) a Cu_2CeIn single crystal and (*2*) $Cu_2Ce_{1.06}In$ polycrystal. The inset shows the magnetisation of the $Cu_2Ce_{1.0}In$ single crystal [87O2].

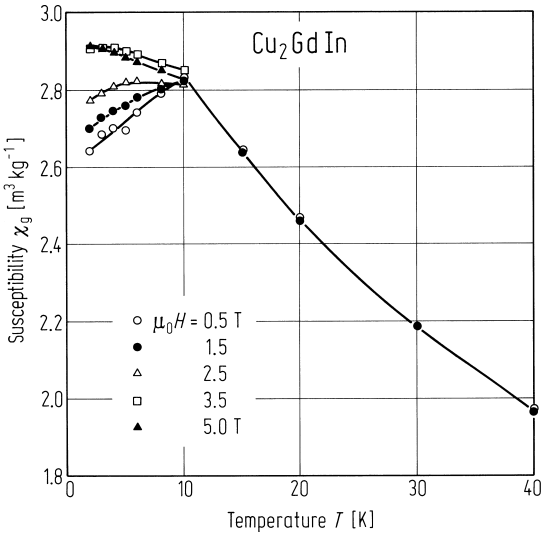

Fig. 156. Static susceptibility of Cu_2GdIn for several applied fields and as a function of temperature [93N1].

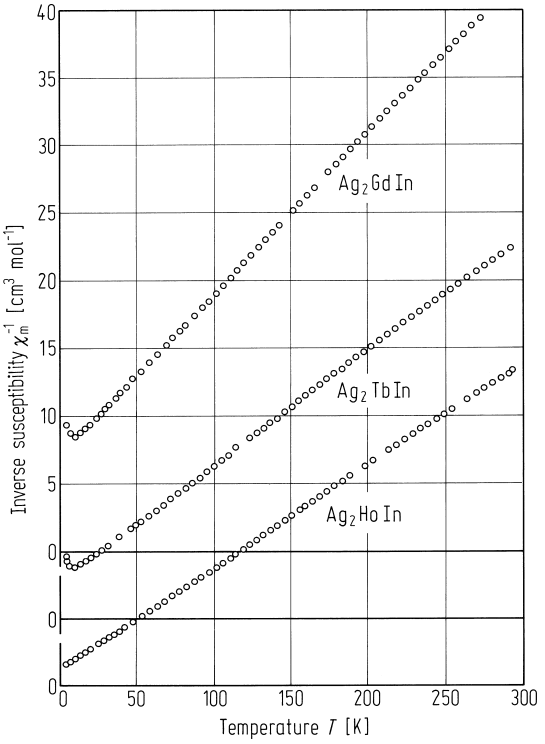

Fig. 158. Thermal variation of the reciprocal susceptibility of Ag_2GdIn, Ag_2TbIn and Ag_2HoIn [84G1].

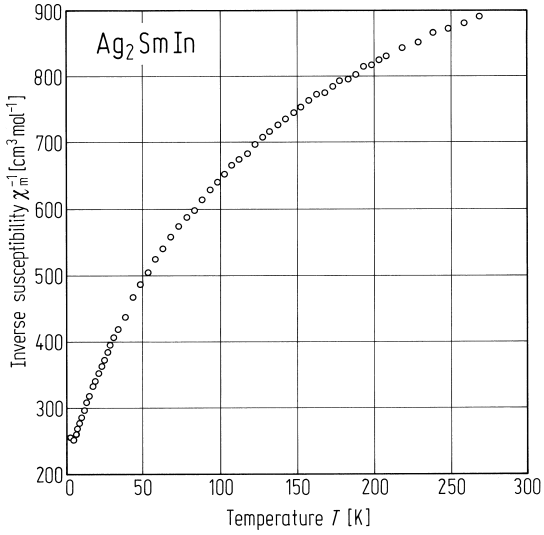

Fig. 159. Thermal variation of the reciprocal susceptibility of Ag_2SmIn indicating the absence of Curie-Weiss behaviour [84G1].

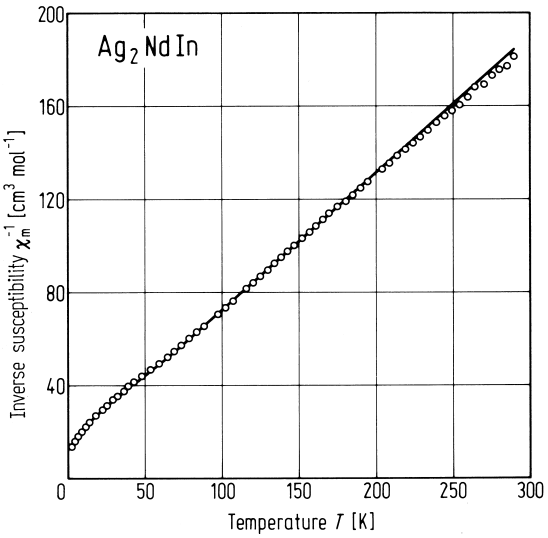

Fig. 160. Thermal variation of the reciprocal susceptibility of Ag_2NdIn. The solid line represents the predictions of a CEF model [84G1].

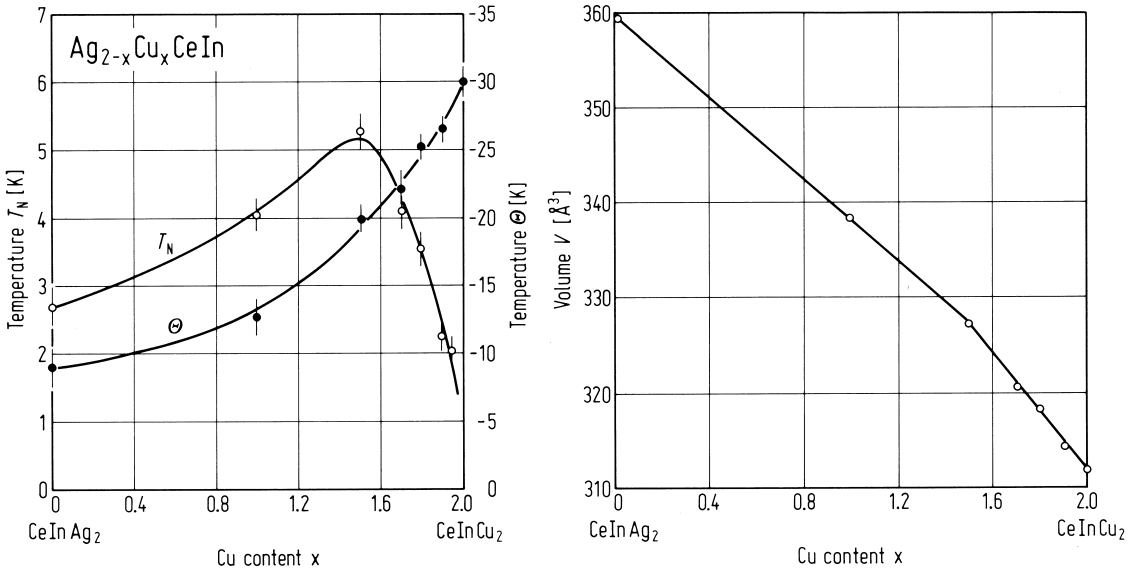

Fig. 161. Paramagnetic Curie temperature Θ, Néel temperature T_N and volume of crystallographic cell of $Ag_{2-x}Cu_xCeIn$ vs. composition [87L1].

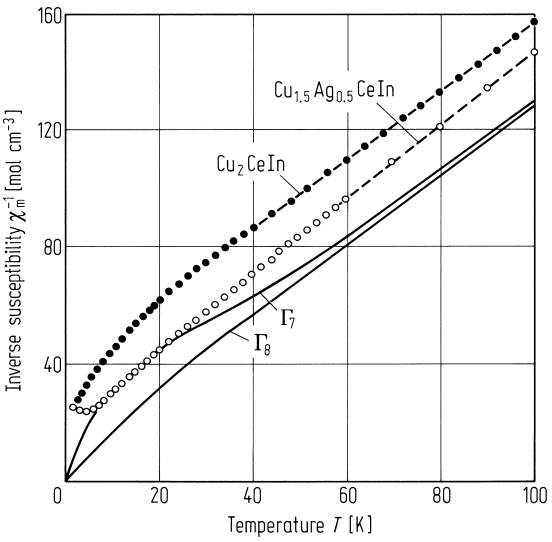

Fig. 162. Reciprocal susceptibilities for $CeInCu_2$ and $CeInCu_{1.5}Ag_{.5}$. The continuous line represents the theoretical variations for a single Ce^{3+} ion and a crystal field splitting Δ = 98 K with either Γ_7 or Γ_8 ground state [87L1].

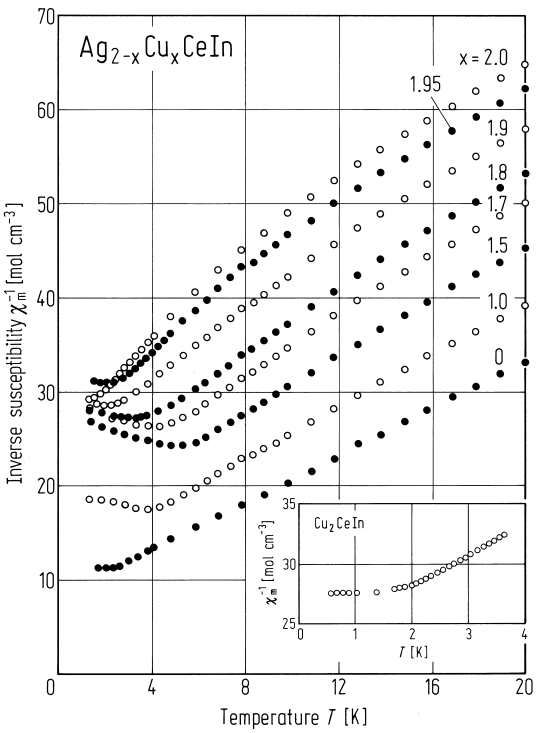

Fig. 163. Reciprocal susceptibilities for Ce compounds in the temperature range 1.5 to 20 K. The inset represents the reciprocal susceptibility for $CeInCu_2$ below 4 K [87L1].

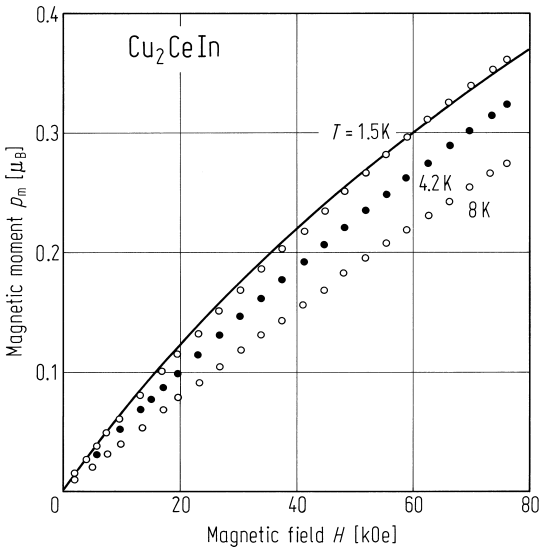

Fig. 164. Magnetic isotherms for a $CeInCu_2$ single crystal along the [100] axis and T = 1,5, 4.2 and 8 K. The continuous line is a fit using T_K = 6.5 K and Δ = 98 K [87L1].

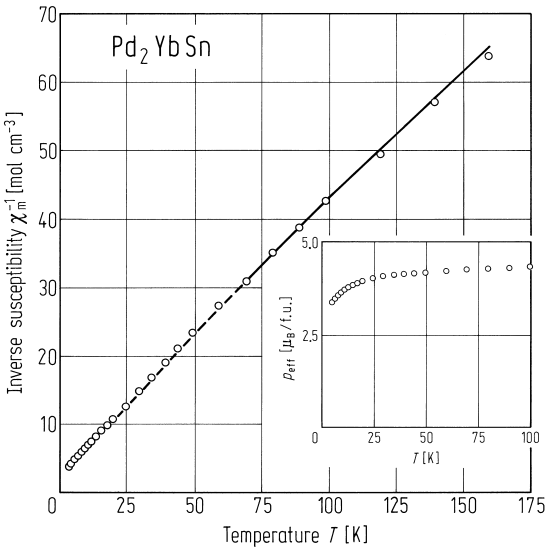

Fig. 165. Thermal variation of the reciprocal susceptibility of Pd_2YbSn. The solid line represents a fit to the data using a CEF model with parameters W = 11.9 K and x = – 0.65 (see subsect. 1.5.5.4.2). The inset shows the temperature dependence of the effective paramagnetic moment [85M1].

Table 31. Magnetic properties of Pd_2(R)Sn alloys [85M1].

Compound	a [Å]	p_{eff} (exp) [μ_B]	p_{eff} (free ion) [μ_B]	Θ [K]	T_N [K]	T_C [K]
Pd_2ScSn	6.503					2.15
Pd_2YSn	6.716					4.55
Pd_2TbSn	6.740	9.05	9.72	– 8.6	9.0	
Pd_2DySn	6.722	10.83	10.85	– 9.3	15.0	
Pd_2HoSn	6.705	10.67	10.61	– 6.2	[a])	
Pd_2ErSn	6.692	9.59	9.58	– 7.6	[a])	
Pd_2TmSn	6.670	7.4	7.56	0		2.82
Pd_2YbSn	6.658	4.34	4.54	– 4.3	0.23 [b])	2.42
Pd_2LuSn	6.645					3.05

[a]) Not ordered magnetically down to 1.4 K.
[b]) Exhibits coexistence of superconductivity and antiferromagnetism.

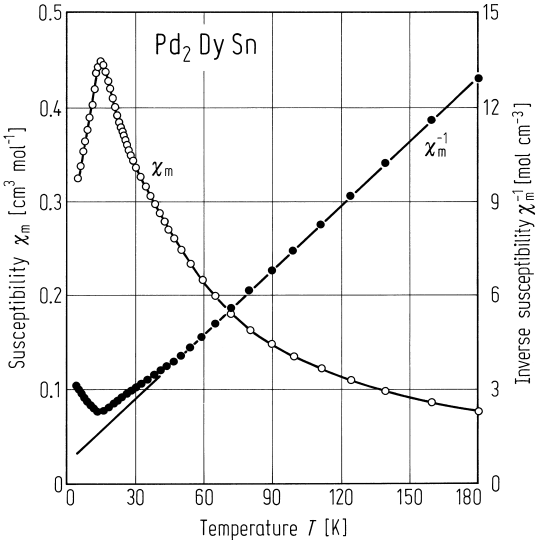

Fig. 166. Susceptibility and reciprocal susceptibility of Pd_2DySn in a field of H = 5 kOe and as a function of temperature. The solid line represents a Curie-Weiss fit $\chi_m = C(T - \Theta)$ to the data [85M1].

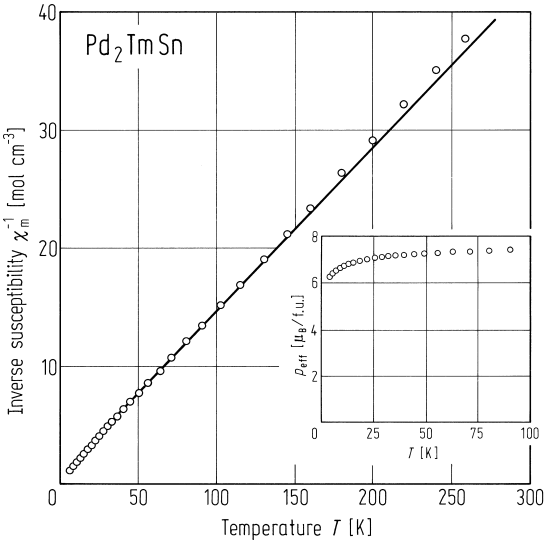

Fig. 167. Thermal variation of the reciprocal susceptibility of Pd_2TmSn. The solid line represents a fit to the data using a CEF model with parameters W = 1.59 K and x = – 0.61 (see subsect. 1.5.5.4.2). The inset shows the temperature dependence of the effective paramagnetic moment [85M1].

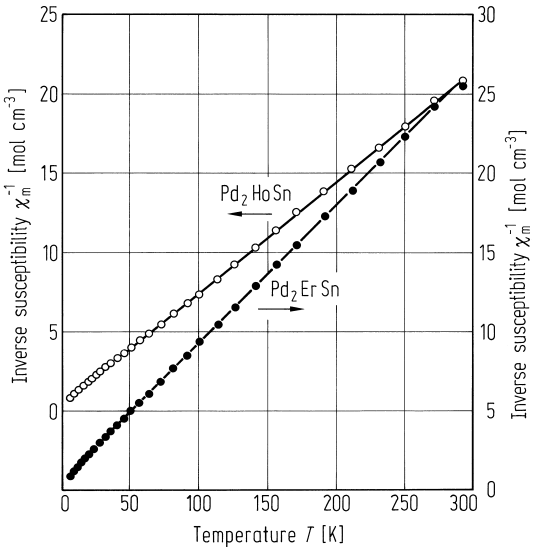

Fig. 168. Thermal variation of the reciprocal susceptibility of Pd_2HoSn and Pd_2ErSn, indicating the absence of magnetic order down to 1.4 K. The susceptibilities are Curie-Weiss in nature with the measured effective Bohr magneton numbers close to the thermal free ion values [85M1].

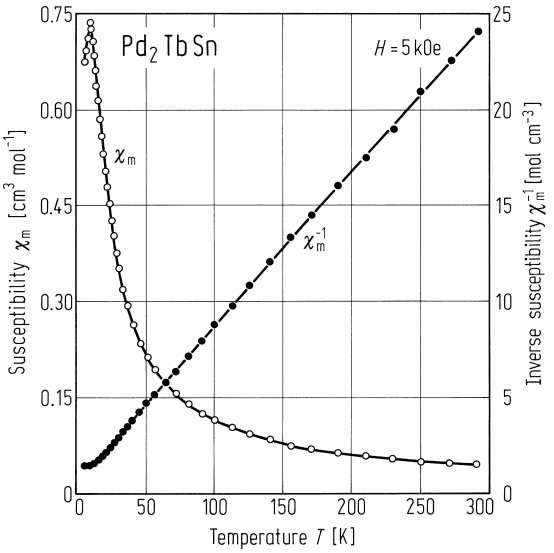

Fig. 169. Susceptibility and reciprocal susceptibility of Pd_2TbSn in a field of H = 5 kOe and as a function of temperature. The solid line represents a Curie-Weiss fit $\chi_m = C/(T - \Theta)$ [85M1].

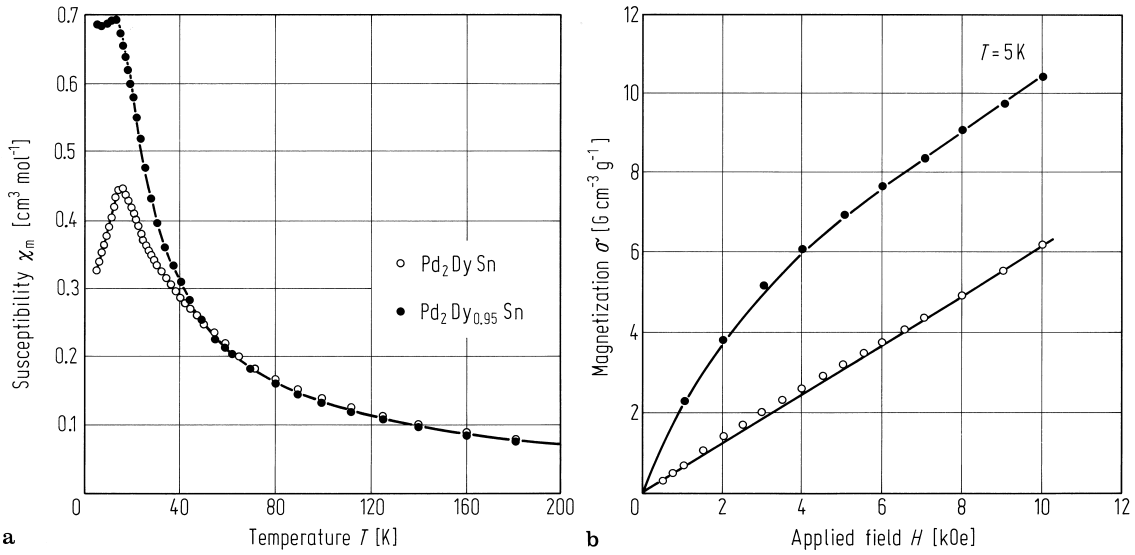

Fig. 170. (**a**) Susceptibility vs. temperature at H = 5 kOe for Pd_2DySn and $PdDy_{0.95}Sn$ and (**b**) magnetisation vs. applied field at 5 K [85U4].

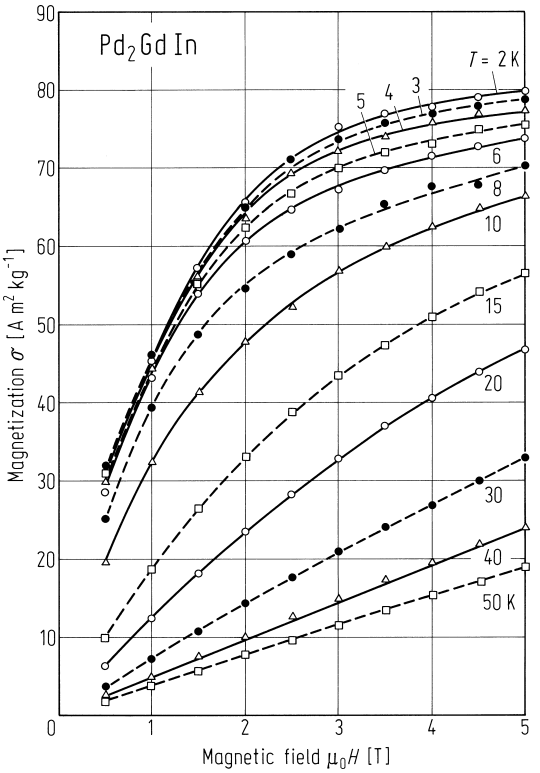

Fig. 171. Magnetic isotherms of disordered Pd_2GdIn. The temperatures are marked on the curves [92N1].

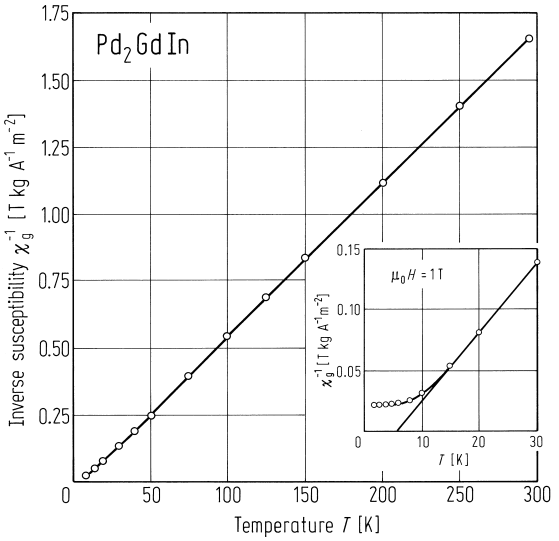

Fig. 172. Inverse susceptibility as a function of temperature for disordered Pd_2GdIn. The data shown in the inset were taken in an applied field of 1 T [92N1].

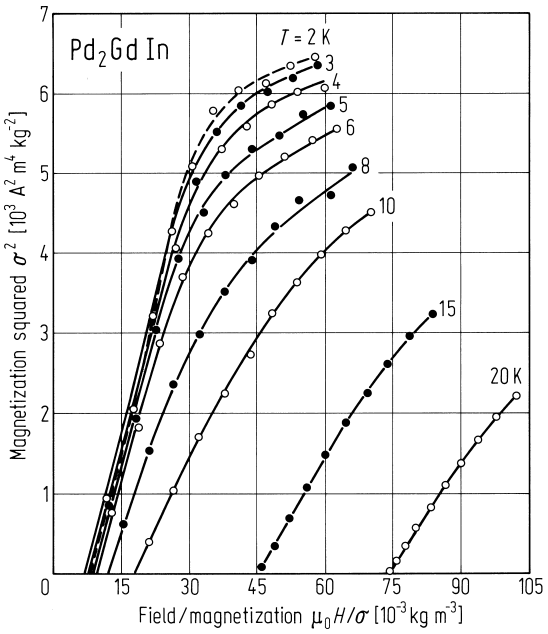

Fig. 173. Magnetic isotherms of disordered Pd_2GdIn. The temperatures are marked on the curves [92N1].

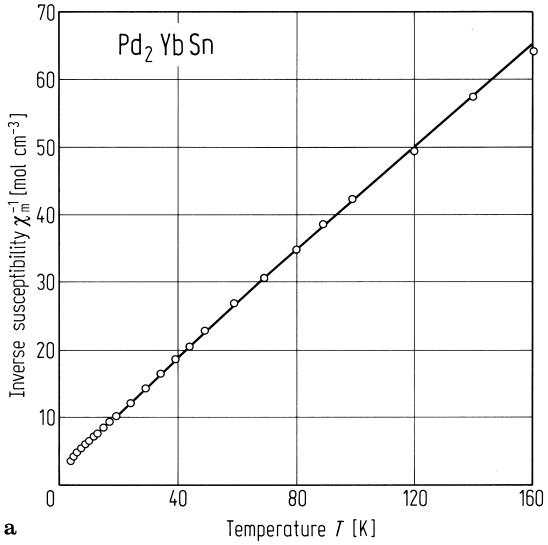

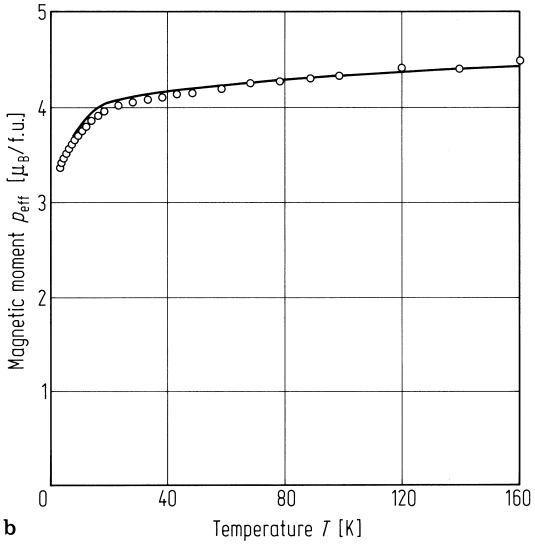

Fig. 174. Inverse susceptibility (**a**) and effective paramagnetic moment (**b**) vs. temperature for Pd_2YbSn. The solid line is a model calculation including crystal field splitting and exchange effects in a mean field approximation [85K1].

R_2AgIn ($RAg_{.5}In_{.5}$)

Atomic size normally excludes the formation of single phase alloys. However, single phase Heusler alloys have been reported with R = Gd, Tb, Dy, Ho, Er, Tm and Yb. The Gd compound is ferromagnetic (T_C = 118 K), Tb and Dy meta-magnetic. T_N = 66 K, 30 K, respectively and Ho, Er, Tm and Yb are ferromagnetic with transition temperatures 24, 22, 21 and 20 K, respectively.

Table 32. Physical properties of (R)$In_{0.5}Ag_{0.5}$ alloys [81L1]. r: R^{3+} ionic radius.

R	r [Å]	a [Å]	V [Å^3]	ρ [g cm^{-3}]	
				X-ray	measured
Gd	0.938	3.716	51.30	8.691	8.707
Tb	0.923	3.702	50.74	8.845	8.847
Dy	0.908	3.685	50.04	9.167	9.015
Ho	0.894	3.666	49.27	9.310	9.247
Er	0.881	3.651	48.67	9.505	9.512
Tm	0.869	3.629	47.79	9.737	9.430

Table 33. Magnetic parameters of some (R)$In_{0.5}Ag_{0.5}$ alloys [81L1]. FM: ferromagnetic, MM: metamagnetic, p: effective paramagnetic moment, p_f: ferromagnetic saturation moment.

		R = Gd	Tb	Dy
Bulk nature		FM	MM	MM
T_o [K]		118	66	30
Θ [K]		120	70	32
C [10^{-5} m^3 K kg^{-1}]		42.7	57.1	70.1
p [μ_B]	theor	7.94	9.72	10.63
p [μ_B]	exp	8.54	9.91	11.05
p_f [μ_B]	theor	7	9	10
p_f [μ_B]	exp	7.61	7.94	9.61

Table 34. Magnetic parameters of some (R)$In_{0.5}Ag_{0.5}$ alloys [81L1]. FeM: ferrimagnetic, C_1, C_2: Curie constants corresponding to the two sublattices of a ferrimagnetic system, p: effective paramagnetic moment, p_f: ferromagnetic saturation moment, Θ_p: paramagnetic Curie temperature. The parameters Θ and Θ_b are obtained by using $1/\chi = (T - \Theta_p)/C - \Theta_b^2/C(T - \Theta)$. The exchange field has been parameterised using $W_{12} = -n$, $W_{11} = \alpha n$, $W_{22} = \beta n$ where α and β are dimensionless constants. d: density.

Alloy		Ho	Er	Tm	Yb
Bulk nature		FeM	FeM	FeM	FeM
C [10^{-5} m^3 K kg^{-1}]		62.5	48.2	31.4	8.25
C_1 [10^{-5} m^3 K kg^{-1}]		52.0	41.5	27.1	7.93
C_2 [10^{-5} m^3 K kg^{-1}]		10.5	6.7	4.3	0.32
Θ_p [K]		– 20	– 25	– 27	– 170
T_N [K]		24	22	21	20
Θ [K]		18.1	16.0	16.0	14.0
Θ_b [K]		16.1	16.8	16.8	33.8
$\alpha = \beta$		– 0.029	– 0.12	– 0.14	– 0.60
n/d		11.5	16.7	25.8	≈ 580
p	exp	10.48	0.24	7.48	3.86
p	theor	10.60	9.60	7.60	4.54

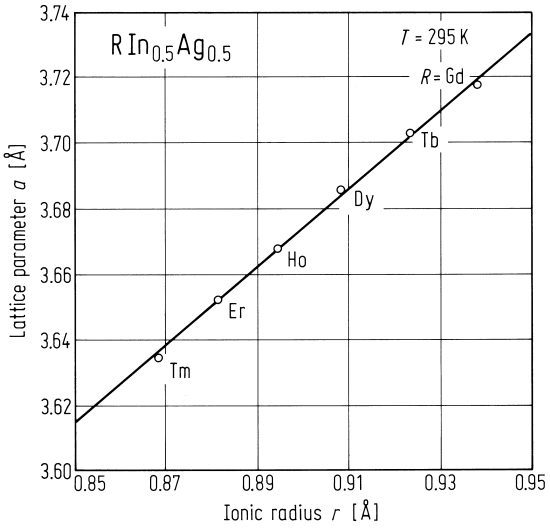

Fig. 175. Lattice parameter vs. rare earth radius for $RIn_{0.5}Ag_{0.5}$ compounds [81L1].

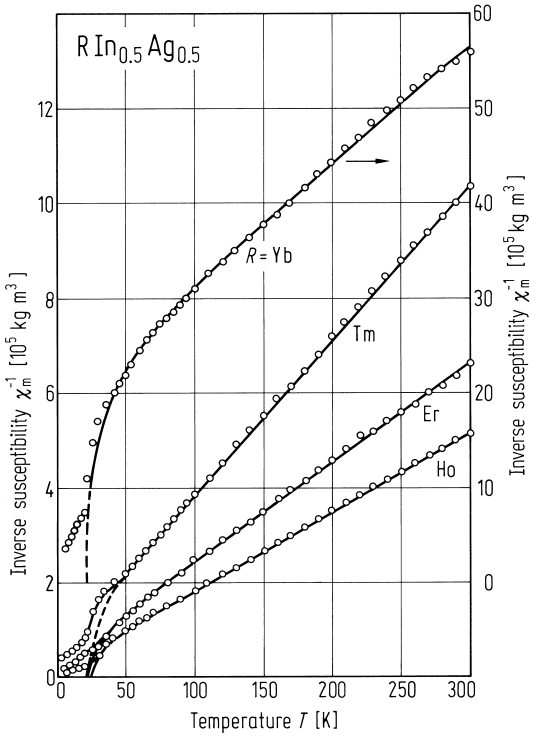

Fig. 178. Inverse magnetic susceptibility vs. temperature for $RIn_{0.5}Ag_{0.5}$ with R = Ho, Er, Tm, Yb [81L1]. H = 320 kAm^{-1} for Ho, Er, Tm and H = 960 kA m^{-1} for Yb.

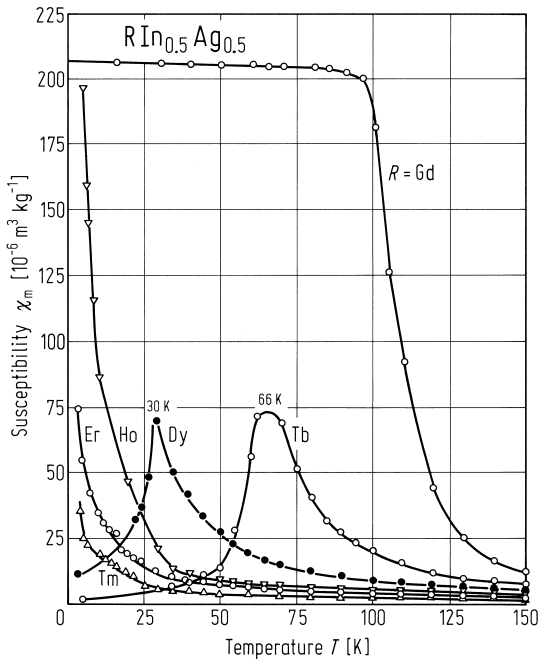

Fig. 176. Susceptibility vs. temperature at H = 320 kAm^{-1} for $RIn_{0.5}Ag_{0.5}$ alloys (R = Gd, Tb, Dy, Ho, Er, Tm) [81L1].

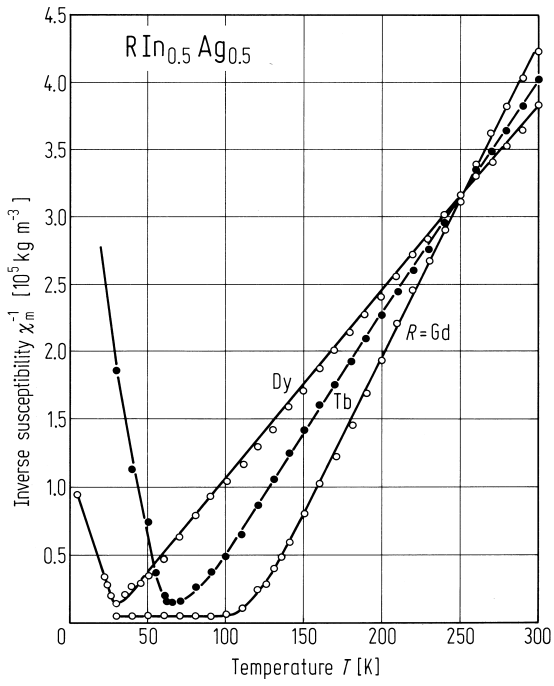

Fig. 177. Inverse magnetic susceptibility vs. temperature at H = 320 kA m^{-1} for $RIn_{0.5}Ag_{0.5}$ with R = Gd, Tb, Dy [81L1].

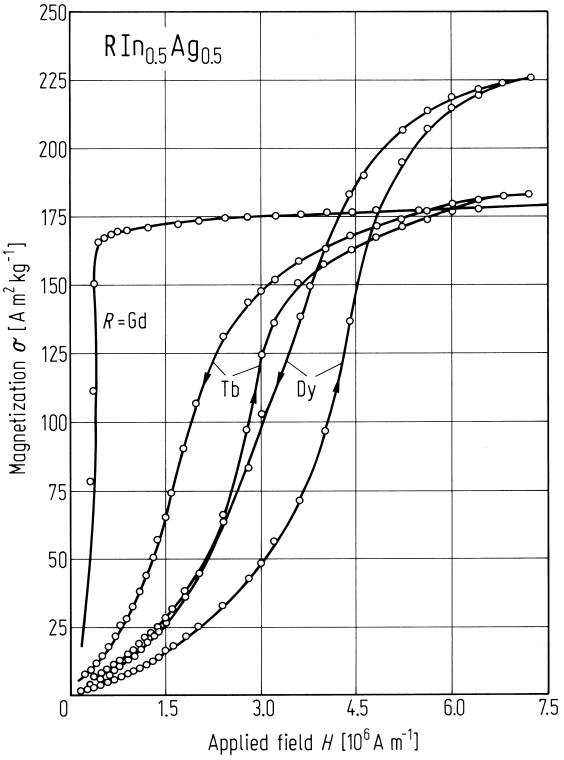

Fig. 179. Magnetisation vs. applied magnetic field for $RIn_{0.5}Ag_{0.5}$ with R = Gd, Tb, Dy [81L1].

1.5.5.3.3.5 Quaternary

The effects of electron concentration on the magnetic properties of Heusler alloys has been investigated in a series of quaternary compounds. Continuous Heusler series form at the intermediate compositions $Pd_2MnIn_{1-x}Sn_x$, $Pd_2MnSn_{1-y}Sb_y$ and $Pd_2MnIn_{1-x}Sb_x$ and the details have been summarised [88W1]. In these series three types of magnetic structure are observed, antiferromagnetic fcc type 2 (AF2), antiferromagnetic fcc type 3A (AF3A) and ferromagnetic. The results show a direct correlation between electron concentration and magnetic structure. Similar behaviour has been observed in the series $Pd_{2-x}Cu_xMnIn$ [88W1] in which substitution is made at the X site rather than the Z site.

$X_2(YY^*)Z$ X = 3d, Y= Y* = 3d

X = 8A: Fe
Y = 7A: Mn
Y* = 5A: V
Z = 4B: Sn

$Fe_2Mn_{1-x}V_xSi$

Single phase compounds with the $L2_1$ structure form for the entire composition range $0 \le x \le 1$. The Curie temperature increases from 219 K for x = 0 to 315 K at x = 0.5. For x > 0.5 the Curie temperature decreases rapidly, vanishing at x = 0.86.